Engineering Fracture Mechanics 176 (2017) 83–99

Contents lists available at ScienceDirect

Engineering Fracture Mechanics

journal homepage: www.elsevier.com/locate/engfracmech

A microstructure-based multisurface failure criterion for the description of brittle and ductile failure mechanisms of clear-wood

Markus Lukacevic *, Wolfgang Lederer, Josef Füssl

Institute for Mechanics of Materials and Structures, Vienna University of Technology, Karlsplatz 13, 1040 Vienna, Austria

ARTICLE INFO

Article history:
Received 16 December 2016
Received in revised form 21 February 2017
Accepted 21 February 2017
Available online 24 February 2017

Keywords:
Wood
Failure mechanisms
Unit cell method
XFEM

ABSTRACT

The failure behavior of wood, a complex natural composite, highly depends on structural features on several lower length scales. Thus, a new approach for the prediction of failure mechanisms of wood is proposed, aiming at a better description of mechanical processes in wood by taking the influence of microstructural characteristics into account.

Previously proposed failure criteria for wooden cells are now linked to unit cells at the annual ring scale. Extensive investigation of load combinations allow the identification and classification of the main failure mechanisms of clear-wood. Based on these findings, a multisurface failure criterion is formulated, indicating brittle as well as ductile failure mechanisms and giving interesting insight into the failure behavior. A new algorithm is presented, which enables the simultaneous description of plastic failure and cracking within numerical simulations. Finally, the failure criterion is validated for biaxial experiments and applied to a timber engineering example.

1. Introduction

The future competitiveness of wood compared to other building materials, like masonry, steel or concrete, highly depends on the development of sophisticated simulation tools. Here, one of the main challenges encountered is the prediction of load bearing capacities based on realistic failure mechanisms. The development of new or optimization of existing wood-based products and the combined use of wood with steel, for example in dowel-type timber connections, requires the description of mechanical processes in wood even after the point of failure. Formation of cracks or ductile mechanisms could be allowed for particular loading situations to better exploit the potential of wood.

Due to the complex microstructure of wood, traditional strength prediction methods are usually not able to capture the mechanisms, close to or after the point of failure, correctly. Frequently used failure criteria for orthotropic materials, which are based on the evaluation of maximum stress or strain values, vastly underestimate the load-carrying capacity of timber elements, as very local peak values not necessarily lead to structural failure, because of stress redistribution effects, such as localized cell wall failure. This fact can be taken into account by the use of so-called mean stress approaches [18,28], where stress values are averaged over finite small areas and then used to estimate the point of structural failure. Various researchers combined this method with findings of linear elastic fracture mechanics and applied it to wood [35,37,38,31]. A closer inspection of actual starting points of failure in experiments showed that, at least on a single board level, the effects of inho-

* Corresponding author.
E-mail address: markus.lukacevic@tuwien.ac.at (M. Lukacevic).

http://dx.doi.org/10.1016/j.engfracmech.2017.02.020
0013-7944/

mogeneities, like knots, cannot be neglected. Thus, the implementation of fiber deviation models [11,12] is the first step toward the consideration of wood specific failure mechanisms. Such an approach led to a new structural failure criterion based on the evaluation of stress states in the vicinity of knots, proposed by two of the authors [23]. Furthermore, the capability of the numerical simulation tool to depict stress- and strain fields in wooden boards with sufficient accuracy was shown in Lukacevic et al. [25]. Like in [33], this simulation tool utilized a classic, orthotropic failure criterion in combination with elastic-plastic material behavior. To overcome limitations of such models, e.g. their inability to capture differences in compressive and tensile behavior very well, several researchers developed multisurface plasticity models for clear wood [27,1] or even combined those with cohesive zone models for the description of brittle failure mechanisms under tensile and shear loading conditions [34]. Dourado et al. [5] combined experimental data and a genetic algorithm in their determination of crack properties in cohesive crack simulations. Cohesive zone models were also used in the investigation of glued laminated timber beams with holes in [3]. Such an approach is limited to applications, where the crack path is obvious beforehand and, thus, can be predefined. A first approach to tackle this problem was presented in [15], where an iterative procedure with a step-by-step insertion of such cohesive elements was used instead of a predefined crack path. The importance of considering structural features for the correct modeling of fracture mechanisms has also been shown in the development of morphological lattice models [7,19,20] and other hierarchical computational models [30,32], where for two-dimensional simulations the explicit representation of early- and latewood was necessary.

In Lukacevic et al. [26] we proposed a new approach, where failure mechanisms are based on detailed material models on lower length scales (see Fig. 1). With such a procedure the amount of fitting parameters and the need for extensive identification experiments should be reduced to a minimum. In the first step of our modeling strategy, failure mechanisms of the two main clear wood layers, late- (LW) and earlywood (EW), were identified at the wood cell level by using an approach based on the XFEM. Only few assumptions on failure mechanisms of cell wall and surrounding material were necessary. The results from an extensive range of loading combinations were then used to derive two multisurface failure criteria for the two cell types, which were already used for simulations and validation at the annual ring level [26,24].

In the present paper, in a next homogenization step, the two new multisurface failure criteria will be applied to a new unit cell at the annual year ring level, where LW and EW will be modeled individually but as homogeneous layers. To allow the simultaneous use of plastic failure and crack initiation surfaces within a commercial FE software, an appropriate algorithm for such multisurface failure criteria has been developed and implemented. Another extensive parameter study on loading conditions then leads to the identification and classification of the main failure mechanisms at the clear-wood level. The results on this length scale are used to obtain a single multisurface failure criterion for clear-wood, where the so-called XFEM-based cohesive segments method is used to describe brittle failure mechanisms under tensile and shear loading, and

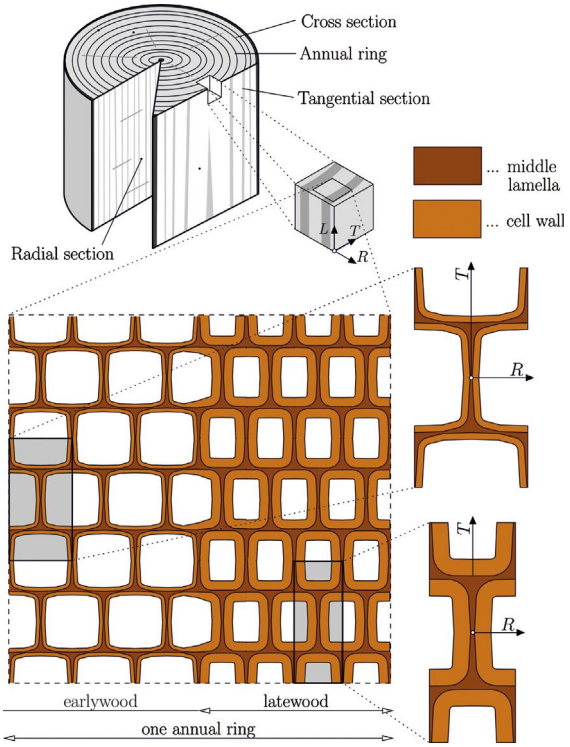

Fig. 1. Modeling approach for the determination of a multisurface failure criteria based on structural features on lower length scales [24].

perfectly plastic behavior to describe ductile failure mechanisms under compression. Thereby, the advantages of both approaches can be combined optimally. Finally, the new failure criterion for clear-wood is validated for biaxial experiments of spruce samples in the longitudinal/radial plane and applied to a dowel-type timber connection [21], showing the simulation tool's capabilities.

2. Material and methods

2.1. Annual year ring model

In the radial-tangential plane, clear-wood, which is defined by being defect free, is made up of a layered structure of mostly early- (EW) and latewood (LW), which are even visible to the naked eye. A single sequence of one of each of these two layer types is called annual year ring. In reality, so-called transition wood can be found in between EW and LW. This additional layer is neglected within the following simulations, as its failure behavior is not decisive. Furthermore, the actually concentrically arranged annual rings are modeled perfectly parallel (see Fig. 2). The annual ring width is chosen with 3 mm and with an EW to LW ratio of 80:20, which conforms to a clear-wood density of 0.46 g/cm^3. The orthotropic stiffness properties for the two layer types were determined by means of a micromechanical model developed and validated by [14]:

$$\mathbb{C}_{EW} = \begin{bmatrix} C_{rrrr} & C_{rrtt} & C_{rrll} & & & \\ & C_{tttt} & C_{ttll} & & & \\ & & C_{llll} & & & \\ & & & C_{rtrt} & & \\ & \text{sym.} & & & C_{rlrl} & \\ & & & & & C_{tltl} \end{bmatrix} = \begin{bmatrix} 8824 & 401 & 508 & & & \\ & 700 & 270 & & & \\ & & 600 & & & \\ & & & 29 & & \\ & \text{sym.} & & & 590 & \\ & & & & & 560 \end{bmatrix} [\text{MPa}] \quad (1)$$

$$\mathbb{C}_{LW} = \begin{bmatrix} 31,880 & 670 & 1080 & & & \\ & 3132 & 1208 & & & \\ & & 2160 & & & \\ & & & 247 & & \\ & \text{sym.} & & & 588 & \\ & & & & & 1236 \end{bmatrix} [\text{MPa}] \quad (2)$$

2.1.1. Multisurface failure criteria for early- and latewood

As mentioned before, in [26] two multisurface failure criteria for EW and LW were developed (see Fig. 3), which represent their effective failure behaviors. In a further development of the models used in [24], now, ductile failure mechanisms under compressive loads are described by using perfectly plastic failure surfaces (see blue surfaces in Fig. 3) and brittle ones under tensile and/or shear loading with crack initiation surfaces (see red surfaces in Fig. 3). Furthermore, to each crack initiation surface an effective crack direction is assigned to. For example, if failure surface $\boxed{1}$ of the EW is active, a crack normal to the local T direction is inserted into the associated element. The applied XFEM-based cohesive segments method uses a traction-separation behavior to describe the crack opening process. After crack initiation, perfect brittle damage evolution is assumed, i.e. the transferable stresses drop almost immediately to zero (displacement from crack initiation to stress free crack surfaces is set to 10^{-5} mm). Additionally, fully cracked elements are still able to transfer stresses over their respective crack surfaces, enabled by a node-to-surface contact formulation with finite sliding. To increase stability of the numerical simulations, damage stabilization with a viscous regularization scheme for the softening part of the traction-separation behavior is applied by defining a viscosity coefficient of 1.0e-4.

2.2. Unit cell method and FE model

To model the repetitive structure of the annual rings, a 3D unit cell with a size of 6 × 6 mm in the RT-plane is defined. Thus, two annual rings in radial direction are modeled (see Fig. 2b), which ensures, especially in the case of brittle failure, that all transition effects from one layer to the other can be captured.

Originally, the unit cell method [29,39,2] has been used to study the elastic response of heterogeneous materials, which are built up of repetitive structural features. By applying periodic boundary conditions, microstress and -strain fields were obtained and the resulting effective stresses used to obtain the materials' stiffness properties. Such an approach has been used in the abovementioned micromechanical model of wood to obtain stiffness properties [14].

The use of unit cells for studying and identifying failure mechanisms has been successfully shown for the development of the multisurface failure criteria of EW and LW in [26]. Thus, the defined unit cell represents the homogeneous material clear-wood.

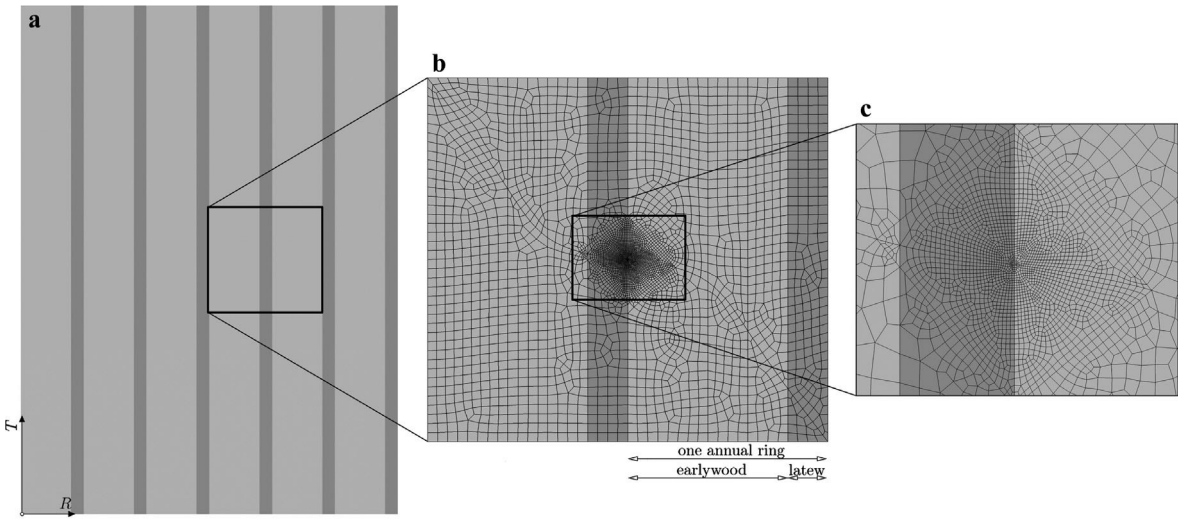

Fig. 2. (a) Layered structure of EW and LW in the RT plane, (b) dimensions, geometry and mesh of the used unit cell, spanning over two annual rings, and (c) detail of the mesh showing the defect (red elements) of the "border" model configuration. (For interpretation of the references to colour in this figure legend, the reader is referred to the web version of this article.)

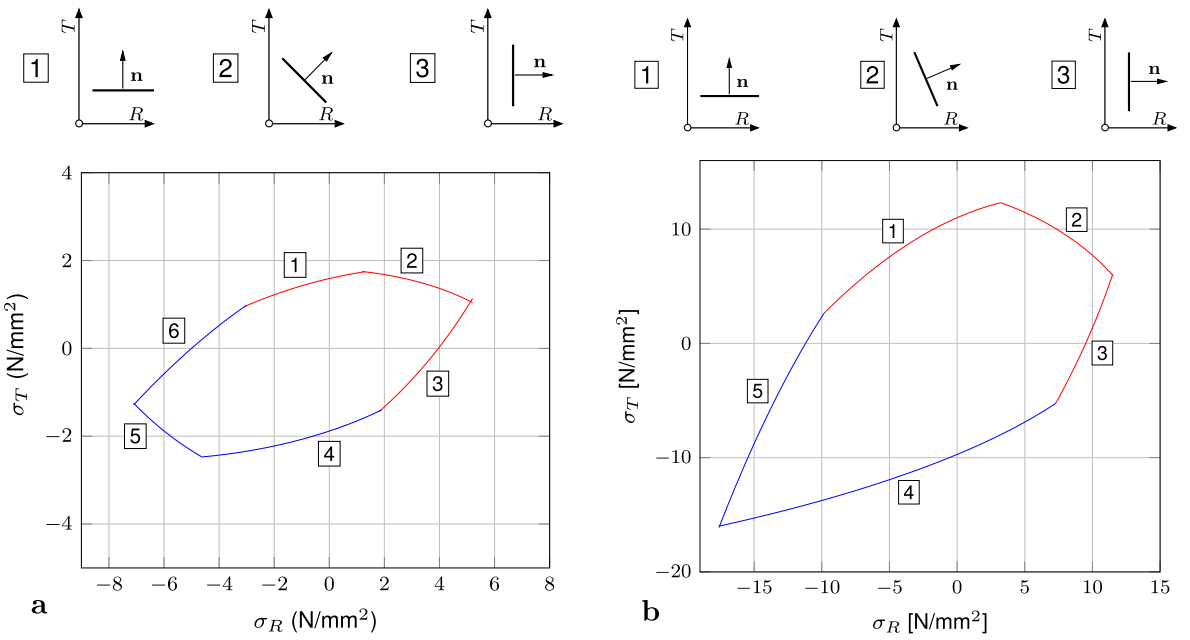

Fig. 3. Failure surfaces for the (a) EW and (b) LW unit cell in the σ_R-σ_T plane, with blue surfaces identifying ductile and red ones brittle failure mechanisms, and for latter ones assigned crack directions after crack initiation are shown (modified from [24]). (For interpretation of the references to colour in this figure legend, the reader is referred to the web version of this article.)

So-called master nodes are used to apply a displacement controlled load onto the unit cell. This would lead to homogeneous stress fields within the two distinctive layers and, thus, no clear point of crack initiation in the case of brittle failure. To overcome this problem, defects as illustrated in Fig. 2c have been introduced, where the strength values were slightly reduced. Without the definition of such a defect, all elements within the critical layer would crack at once and no reliable global crack direction could be obtained. With such defects, now, a clear starting point for a single crack is predefined. As the location of the defect highly influences the failure mechanism, and as previous to the simulations no information is available regarding which layer will fail first, three different defect locations were investigated. Defects of approximately 0.01 mm in length in the middle of one of the two respective layer types (later referred to as LW and EW model) as well as a defect at the border between the two layers (see Fig. 2c for the "border" model). All simulations were realized via 8-

node linear brick elements, resulting in model sizes from 8022 to 9208 elements. The thickness of the unit cell (length in global longitudinal direction) was set to 0.3 mm, as parameter studies showed that larger thicknesses resulted in the same failure mechanisms for the examined loading conditions and as the main focus of the brittle failure mechanisms with varying global crack directions is in the RT-plane.

2.3. Simulation program

The goal of the developed simulation program was to obtain all possible failure mechanisms of clear-wood for any arbitrary loading combination, i.e. tensile, compressive and shear loading, as well as any combination of these. Thus, in an analogous manner to [26], first, in preliminary simulations the extreme values for the applied displacements for the three normal and the three shear directions, respectively, were identified. Next, the Latin hypercube sampling method was used to create a total of 1000 different combinations of the six applicable displacements. This sampling technique ensures that the resulting effective stress states of the unit cell are evenly distributed and cover all possible failure mechanisms.

All simulations were conducted on a high-performance computing cluster with a total of three nodes, with two Intel Xeon E5-2640 (2.50 GHz) CPUs (twelve cores) and 256 GB of RAM each.

For each simulation, the resulting reaction forces are averaged over the unit cell's exterior faces to obtain averaged stresses. For the brittle failure mechanisms the resulting stress curves, plotted as functions of the simulation time increment or the respective averaged strains, could be used to clearly identify the point of failure. For the ductile failure mechanisms up to two critical points for each simulation could be identified and will be discussed in detail in the results section.

3. Calculation

The multisurface failure criteria with the simultaneous use of ductile and brittle failure mechanisms was implemented into commercial FE software, using various different user subroutines. The developed algorithm, which allows the use of multiple and, especially, very differing failure surfaces with regard to their failure mechanisms, is here described briefly and also illustrated in the flowchart in Fig. 4.

The procedure and sequence of the different user subroutines stays the same throughout the whole analysis until the first crack occurs. At the start of every increment the status of the enriched elements, i.e. those elements, in which cracking is allowed, is accessed with the help of a python script, which reads the output database of the corresponding FE simulation, in order to identify the already cracked elements. Information on the crack status of elements is essential for the further calculation process and therefore passed into the material user subroutine, which is mainly used to define material behavior. Here, the main part of the multisurface material model is embedded, and the mechanical constitutive behavior of the material is defined. This subroutine is called at all integration points of the elements at every increment. In addition to the predetermined crack status of all elements, total strain components and strain increments are transferred. At the end of this subroutine the stresses and the solution-dependent state variables are updated and the material Jacobian matrix $\partial\Delta\sigma/\partial\Delta\epsilon$ for the mechanical constitutive model is calculated and returned to the other subroutines as well as to the main program. At the beginning of the material user subroutine the orthotropic elastic stiffness tensors of all used materials are defined.

The implemented return mapping algorithm is based on additive decomposition of the strain tensor $\boldsymbol{\varepsilon}$ in an elastic strain part $\boldsymbol{\varepsilon}^e$ and a plastic strain part $\boldsymbol{\varepsilon}^p$, according to the relationship

$$\boldsymbol{\varepsilon} = \boldsymbol{\varepsilon}^e + \boldsymbol{\varepsilon}^p. \tag{3}$$

At the beginning of the algorithm and as an input for the following linear elastic predictor step, the total strain at the end of the increment $\boldsymbol{\varepsilon}_{n+1}$ is calculated as the sum of the transferred total strain components and the strain increments. This implies that frozen plastic flow is assumed for the linear elastic predictor step. Therefore, this step yields the trial stress state at the end of the current increment as

$$\boldsymbol{\sigma}^{trial}_{n+1} = \mathbf{C}(\boldsymbol{\varepsilon}_{n+1} - \boldsymbol{\varepsilon}^p_n), \tag{4}$$

with $\boldsymbol{\varepsilon}^p_n$ as the plastic strain at the start of the increment. This plastic strain at the start of the current increment is equal to the calculated plastic strain at the previous increment, which has been stored as a solution-dependent state variable.

In some situations, especially due to the nature of the used failure surfaces (e.g. closed failure surfaces), it might be advisable to restrict the range of single surfaces by defining respective lower and/or upper stress limits. With the trial stress state the active failure surfaces, which are the ones not violating the predefined limits, are identified and the information is stored in the array s_α (1 . . .active, 0 . . .not active). In the next step, the algorithm checks, if the trial stress state is in the elastic stress region or if a failure surface is reached by evaluating the failure criteria for all active failure surfaces:

$$f^{trial}_{\alpha,n+1} = f_\alpha(\boldsymbol{\sigma}^{trial}_{n+1}) \qquad \alpha \in \{1,\ldots,n_f\} | s_\alpha > 0, \tag{5}$$

with n_f being the number of failure surfaces. Next, the array $f_{\alpha,v}$ is compiled

$$f_{\alpha,v} = 1.0 \quad \text{if} \quad f^{trial}_{\alpha,n+1} > 0 \qquad \alpha \in \{1,\ldots,n_f\}, \tag{6}$$

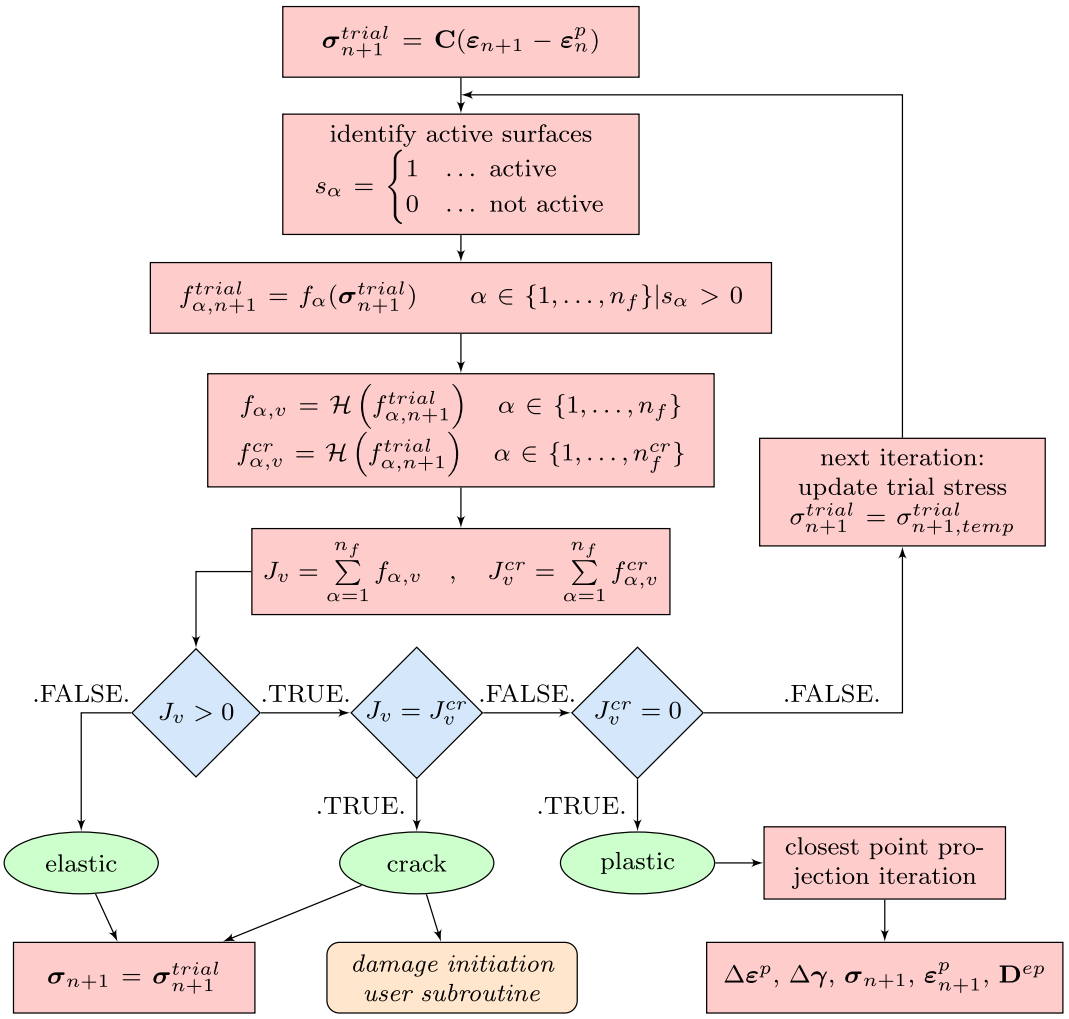

Fig. 4. Flowchart of the decision procedure of identifying the existing process within the material user subroutine.

containing information of which failure criterion is violated. With, in our case, the failure surfaces $f_\alpha(\boldsymbol{\sigma})$ being based on the quadratic formulation of the failure criterion of Tsai and Wu [40]

$$f(\boldsymbol{\sigma}) = a_{ij}\sigma_{ij} + b_{ijkl}\sigma_{ijkl} - 1 \leqslant 0, \tag{7}$$

now, the first and second derivatives of the failure criteria can be calculated:

$$1^{\text{st}} \text{ derivative} : \partial_{\boldsymbol{\sigma}} f_\alpha = a_{ij,\alpha} + 2 \cdot b_{ijkl,\alpha} \cdot \sigma_{ij} \alpha \in \{1,\dots,n_f\} \tag{8}$$

$$2^{\text{nd}} \text{ derivative} : \partial^2_{\boldsymbol{\sigma}\boldsymbol{\sigma}} f_\alpha = 2 \cdot b_{ijkl,\alpha} \alpha \in \{1,\dots,n_f\}. \tag{9}$$

With the calculated values of the failure criteria of all active failure surfaces it is already possible to distinguish if the current step is an elastic one or if a crack or plastic process exist:

$$f_{\alpha,n+1}^{trial} < 0 \text{ for } \textbf{all} \alpha \in \{1,\dots,n_f\} | s_\alpha > 0 \Rightarrow \textbf{elastic} \tag{10}$$

$$f_{\alpha,n+1}^{trial} \geqslant 0 \text{ for } \textbf{some} \alpha \in \{1,\dots,n_f\} | s_\alpha > 0 \Rightarrow \textbf{plastic/crack} \tag{11}$$

The step is an elastic one, if the trial stress state lies within all the failure surfaces. If at least one failure criterion is violated, this characterizes either a cracking process or a plastic loading condition. To definitely define the actual kind of failure process (crack or plastic) further algorithmic processes are required. With the information, stored in $f_{\alpha,v}$, which failure criteria are violated, the total number of violated failure surfaces J_v and the number of violated crack failure surfaces J_v^{cr} are computed:

$$J_v = \sum_{\alpha=1}^{n_f} f_{\alpha,v} \qquad J_v^{cr} = \sum_{\alpha=1}^{n_f} f_{\alpha,v}^{cr}, \tag{12}$$

which makes it possible to identify three different scenarios:

$$J_v = J_v^{cr} \Rightarrow \textbf{crack} \text{ process} \rightarrow \text{elasticstress} \tag{13}$$
$$J_v^{cr} = 0 \Rightarrow \textbf{plastic} \text{ process} \tag{14}$$
$$J_v \neq J_v^{cr} \neq 0 \Rightarrow \text{iterationtodefineinnermost(decisive)failuresurface.} \tag{15}$$

In the first two scenarios all violated failure surfaces are solely either crack or plastic surfaces, so that the predominant failure mechanism is clearly defined. The third scenario deals with the possibility that at least one crack and one plastic surface are violated simultaneously, so that a further iteration process is necessary to decide the predominant failure mechanism at this time step. During this iteration process, the innermost violated failure surface for the trial stress state is identified and consequently defines the failure mechanism (crack initiation or plastic process). The main idea of the iteration process is to define a lower (σ_{low}) and an upper (σ_{up}) bound for the stress state, which initially are the trial stress state and the unloaded initial stress state. A temporary stress state as the median of the two bounds is defined for which the failure criteria are checked again, resulting in a new set of violated failure surfaces for this temporary stress state:

$$J_{v,temp} = \sum_{\alpha=1}^{n} f_{\alpha,v} \qquad J_{v,temp}^{cr} = \sum_{\alpha=1}^{n} f_{\alpha,v}^{cr}. \tag{16}$$

With this information it is possible to identify four possible solutions for this iteration step:

$$J_{v,temp} = 0 \Rightarrow \sigma_{low} = \boldsymbol{\sigma}_{n+1,temp}^{trial} \rightarrow \text{nextiteration} \tag{17}$$
$$\left.\begin{array}{l} J_{v,temp} > 0 \\ \text{and} \\ J_{v,temp}^{cr} = 0 \end{array}\right\} \Rightarrow \textbf{plastic} \text{ process} \tag{18}$$
$$J_{v,temp} = J_{v,temp}^{cr} \Rightarrow \textbf{crack} \text{ process} \tag{19}$$
$$J_{v,temp} \neq J_{v,temp}^{cr} \neq 0 \Rightarrow \sigma_{up} = \boldsymbol{\sigma}_{n+1,temp}^{trial} \rightarrow \text{nextiteration.} \tag{20}$$

The iteration routine causes the two bounds to converge to a stress state with only one violated failure surface. This ultimately results in defining the predominant process, which can either be an elastic, a crack or a plastic process.

For an elastic process, which is defined by no violation of any failure surface, the stress state at the end of the increment is set to the trial stress state ($\boldsymbol{\sigma}_{n+1} = \boldsymbol{\sigma}_{n+1}^{trial}$) and the orthotropic elastic stiffness tensor is set to be the material Jacobian matrix:

$$\frac{\partial \Delta\sigma}{\partial \Delta\epsilon} = \mathbf{C}. \tag{21}$$

If the innermost failure surface is a crack surface the predominant failure mechanism is a crack process and the damage initiation user subroutine is invoked, where crack initiation and crack direction are controlled. In the user subroutine, which governs the material behavior, a crack process induces the same procedure as an elastic one, which is why the trial stress state is again set to be the stress state at the end of the increment.

In case of a plastic process, the closest point projection iteration for a general non-smooth yield surface [36,27] has been implemented into the user subroutine. This approach for the application of small strain orthotropic plasticity to a multisurface failure criterion was described briefly in [24] and will be discussed in more detail in a follow up paper.

As this algorithm and, thus, the identification of the correct failure process is repeated for each increment and at all integration points, it allows the process to change in the course of a simulation. For example an integration point's stress state

can move on one of the plastic surfaces until it reaches a crack initiation surface, where finally a crack is introduced into the corresponding element. This capability is especially important for simulations with multiple subsequent loading steps.

4. Results

The failure stress states in three different stress planes for all simulations of the unit cell are shown in Fig. 5. There, the colors indicate the type of failure (the yellow/red colormap denotes brittle and the green/blue one ductile failure) as well as the magnitude of the in-plane shear component τ_{RT} (red and blue ends of the colormaps account for high in-plane shear stresses), and the size of the points correlates to the magnitude of longitudinal shear (the bigger the points the higher the sum of τ_{LR} and τ_{LT}). As already shown in [26], here again a clear envelope of all failure stress states can be defined, where

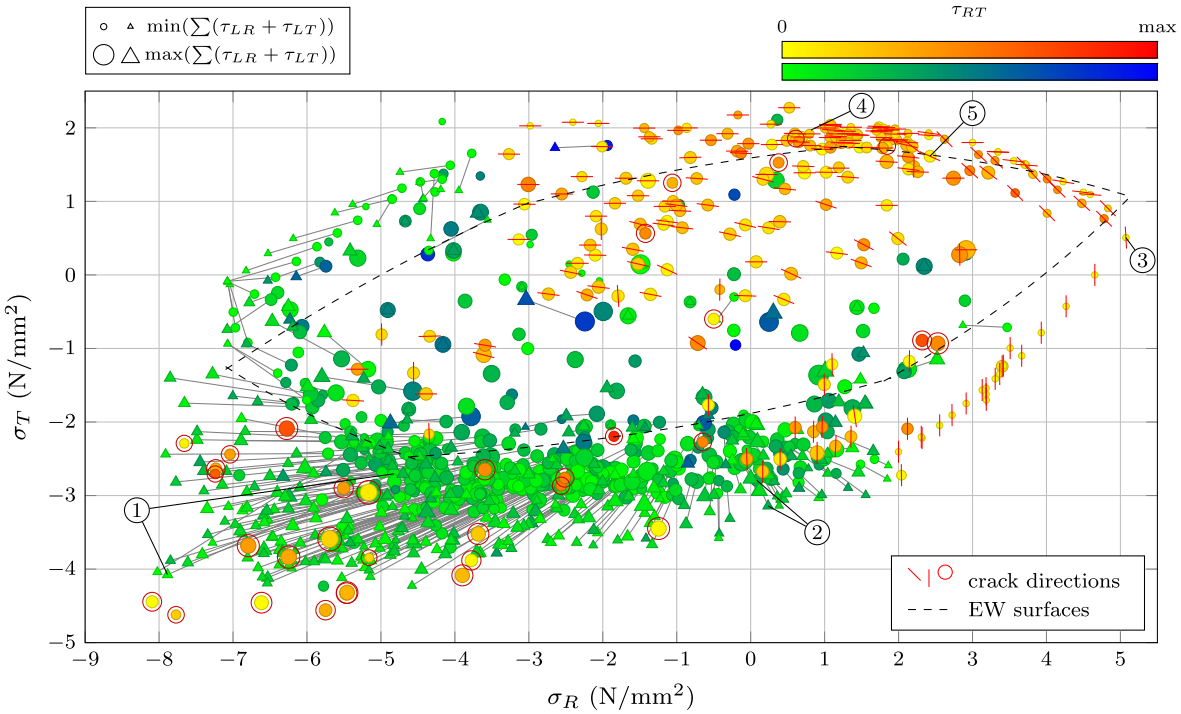

(a) Failure stress states in the σ_R-σ_T plane.

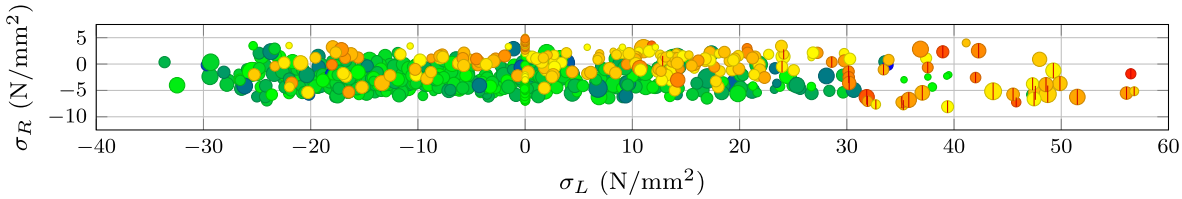

(b) Failure stress states in the σ_L-σ_R plane.

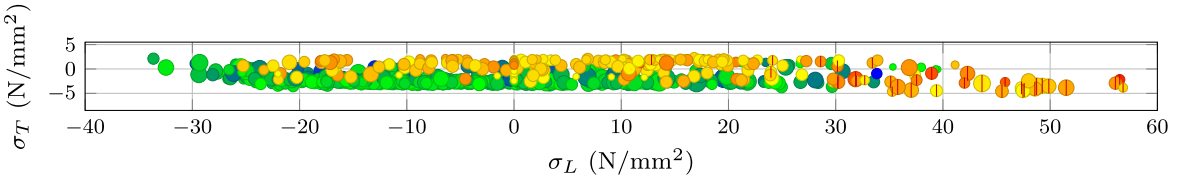

(c) Failure stress states in the σ_L-σ_T plane.

Fig. 5. Failure stress states obtained from simulations of the clear-wood unit cell plotted in several stress planes (the yellow/red colormap indicates brittle and the green/blue one plastic failure mechanisms; the bigger the points the higher the sum of τ_{LR} and τ_{LT}, and the colors indicate the shear stress τ_{RT} according to the colorbar; the red lines indicate the global crack direction of brittle failure mechanisms, with the crack plane being normal to the examined stress plane and in (a) the red circles indicate a crack plane parallel to the examined plane). (For interpretation of the references to colour in this figure legend, the reader is referred to the web version of this article.)

the points close to this envelope are smaller and more towards to the yellow/green end of the colormaps, which means that the corresponding shear stresses are rather low. This means that the presence of shear stresses lowers the maximum failure stresses in the normal directions. The dashed curves in Fig. 5(a) show the previously obtained failure surfaces for EW, whose extreme values lie much closer to the new results than the LW failure surfaces, which would lie outside the plot's axes limits. By comparing these surfaces to the current failure stress states, it can be noticed that especially in tangential direction for both tension and compression higher strength values were achieved for the layered structure. This can be explained by the reinforcement effect of the thinner but stiffer LW layers in this direction as here the two layers are in parallel. Especially in the tensile part of the radial direction, this effect is almost non-existent as here the two layers are in series and the lower strength of EW is decisive.

4.1. Identification of failure mechanisms

The results of the simulation program are now used to identify the main failure mechanisms, which can be primarily distinguished into ductile and brittle failure mechanisms. For the latter ones, additionally, failure modes with distinctive global crack directions can be obtained. By classifying the failure modes, a crucial step towards the following determination of failure surfaces for each failure mode is made, which will lead to a single multisurface failure criterion at the clear-wood level.

4.1.1. Ductile failure

The stress states indicating ductile failure mechanisms are plotted in Fig. 5(a) with a green/blue colormap. As an additional information, for each simulation two stress states are shown, where the first stress state is depicted with a filled circle and the second one with a triangle, and both connected by a gray line. At the first stress state (circles) all elements within the EW layer are fully plastified, whereas at the second stress state (triangles) all LW elements failed by reaching one of the plastic failure surfaces. By examining the distances between the stress states belonging together, it can be noticed that for loading conditions of combined compression in both radial and tangential direction, the distance between the first and second marked stress state is rather big, compared to those stress states with pure compression in only one direction, i.e. those closer to the brittle failure stress states. An example for the former failure mechanism with bigger distance between the two stress states are ones marked with ∘1 in Fig. 5(a). The corresponding stress/strain curves in radial and tangential direction can be seen on the left of Fig. 6. After the first stress state (marked by the circle) is reached, a clear non-linear material behavior can be noticed, which is caused by the completely plastified EW layer. This behavior continues until the LW layer is also fully plastified, which occurs at the points marked with triangles and almost double the stress in radial direction σ_{RR}. At this point the whole unit cell is fully plastified and an perfectly plastic material behavior can be observed in the stress/strain curve. The comparison of the just described failure stress states to the before mentioned EW failure surfaces shows that the points marked with circles lie again close to the dashed curves, but now, due to the just mentioned hardening mechanisms, the corresponding triangles lie far-off for almost all simulation results.

The second example of ductile failure is seen on the right of Fig. 6 and marked with ∘2 in Fig. 5(a). Here the distance between the two marked points is rather small and the non-linear behavior in-between them, in the stress/strain curve, hardly exists. This results in an almost ideally elastic-perfectly plastic material behavior for pure compressive loading in tangential direction.

In summary, this means that although the underlying multisurface failure criteria for the two modeled layers LW and EW themselves only allow linear elastic-ideal plastic failure mechanisms, the application of the two to the layered structure and the nature of the FE model cause the observed hardening effects under combined compression in radial and tangential direction (see stress states/simulation results in lower left region of Fig. 5(a)). The same behavior can be observed for a pure compressive loading in longitudinal direction (see on the left of Fig. 7), where the two layers are also arranged in parallel. After a deflection from the linear material behavior at the first marked stress state, almost an additional 100% of the load can be applied before ideal plasticity is reached.

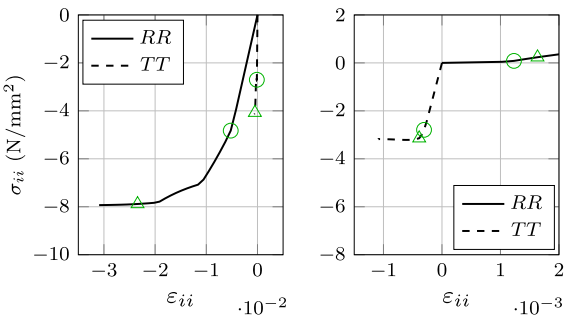

Fig. 6. Stress/strain curves for two exemplary ductile failure mechanisms; the left subfigure corresponds to the stress states marked with 1 in Fig. 5(a) and the right one to stress state 2.

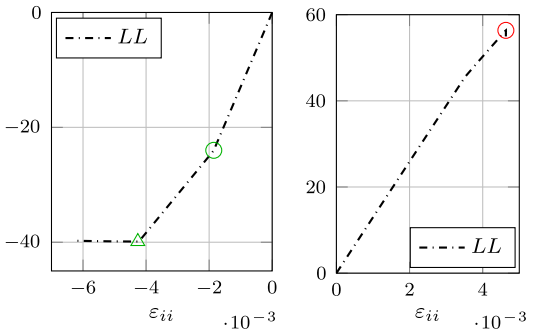

Fig. 7. Stress/strain curves for two exemplary failure mechanisms caused by longitudinal loading conditions (compressive loading on the left and tensile one on the right).

This information can be utilized in the future for the determination of the failure surfaces for the ductile failure mechanisms. In regions with clear linear elastic-ideal plastic material behavior, failure surfaces causing the same material response should suffice, whereas in regions with clearly identifiable hardening effects, the definition of failure surfaces, changing with higher strain values and, thus, depicting the hardening effect might be essential to realistically simulate clear-wood failure mechanisms in such stress regions.

4.1.2. Brittle failure

As mentioned before, for each loading condition three different models were simulated (EW, LW and border model). For ductile failure mechanisms, as expected, all three models yielded exactly the same results due to the nature of the unit cell and the periodic boundary conditions. For the brittle failure mechanisms, the position of the predefined defect is essential, as it determines if the resulting failure mode is realistic or not. Thus, for all loading conditions always the one (out of the three models) which failed first and formed realistic failure modes was chosen. Similar to the evaluation in [26], in this section the main focus lies on the identification of the crack directions within the RT stress plane under arbitrary loading conditions. By concentrating on the results with low shear stress components, we now look at the failure stress states on the imaginary outer envelope, for which just the stress components σ_R and σ_T are not close to zero.

For each simulation the associated illustration of the cracked unit cell is generated automatically at the determined point of failure. Three main failure mechanisms could be observed and are shown in Fig. 8: as expected the global crack direction under radial loading (point ∘3 in Fig. 5(a)) is normal to this direction, i.e. a vertical crack on left of Fig. 8 can be noticed. Here the crack remains within the EW layer, which can be observed in experiments [8,17] and was also shown in preliminary simulations of micro-wedge splitting tests of specimens with special focus on the RT plane [24]. The corresponding stress/strain curves show that the point of failure (marked with circles) can be clearly identified. The second failure mechanism (see middle column of Fig. 8 and point ∘4 in Fig. 5(a), respectively) occurs under predominantly tangential loading. This completely straight crack normal to the tangential direction can also be found in experiments [8,17], where it is caused by the perfectly straight alignment of the single wood cells in this direction (see Fig. 1 on the left). Fig. 5(a) shows that the region, where this kind of failure mode occurs extends quite far to the radial compression region, with values close to $\sigma_T = -2.5$ N/mm^2 and, thus, substantial amounts of tangential compression.

Under combined radial and tangential tensile loading, the resulting global crack direction has an angle between the R and T-directions (see right column of Fig. 8 and point ∘5 in Fig. 5(a), respectively). Within the LW layer the crack path is normal to the layered structure, whereas within the EW the crack deviates from this direction to form the previously mentioned angle between the R and T-directions. As the EW layer is much thicker than the LW layer, also the effective global crack direction is not completely horizontal. A closer look into the variation of this crack angle, shows that an absence of shear stresses (see stress states close to the imaginary outer envelope in Fig. 5(a)) results in smaller angles to the global R direction, whereas an even small presence of shear stresses cause steeper crack angles of up to 45 degrees.

Under tensile loading in global longitudinal direction (see stress states with red circles around them in Fig. 5(a)), a crack normal to this direction could be observed. The corresponding stress/strain curves can be seen on the right of Fig. 7. In contrast to the compressive loading in the longitudinal direction, here only a slight non-linear behavior before the point of failure can be noticed. Although here again the two layers, EW and LW, are arranged in parallel, once the former one fails, it cannot transfer any loads from this point on. Thus, the stresses in the remaining LW layer increase significantly, causing it to fail shortly after. Additionally, it must be noted that it seems like some of the stress states with tensile failure in L-direction plotted in Fig. 5(a) can be found in the lower left and, thus, ductile-failure-prone region. This can be explained by the implementation of the multisurfaces into the FE software. The mentioned failure stress states first fail due to plastic processes and then move on the respective plastic failure surfaces until the crack initiation surface in L-direction is reached. To obtain more points for the identification of the respective crack initiation surface for the global longitudinal crack, brittle

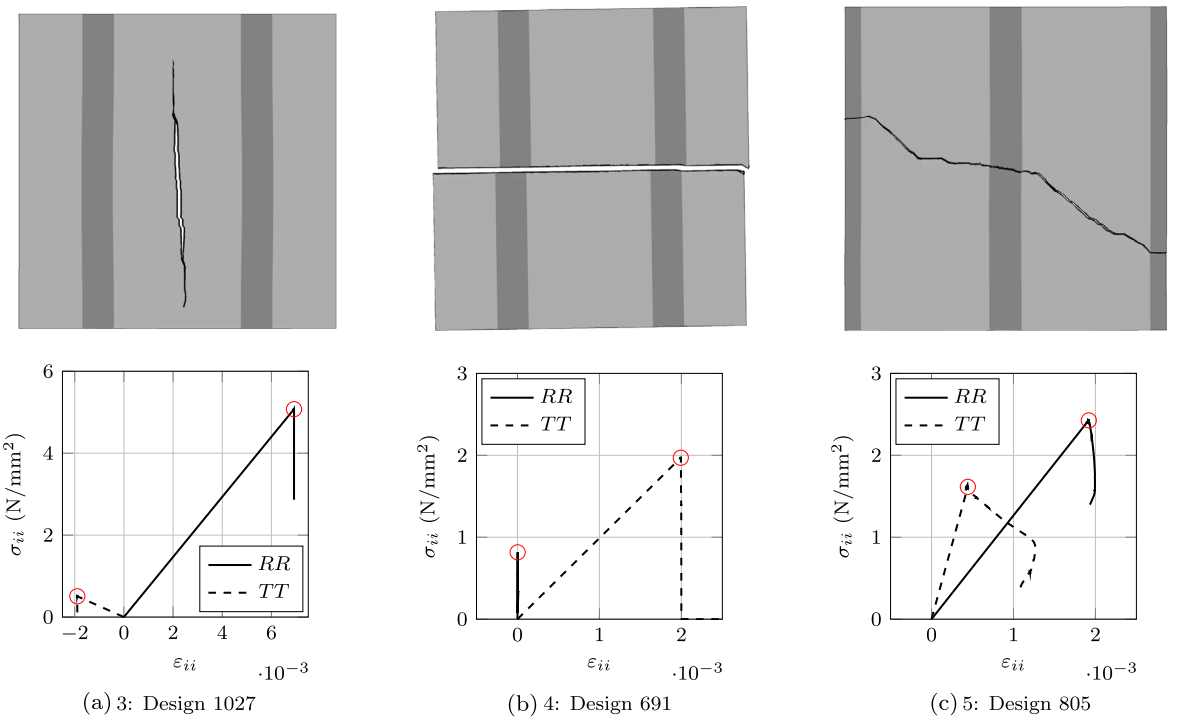

(a) 3: Design 1027 (b) 4: Design 691 (c) 5: Design 805

Fig. 8. Brittle failure mechanisms.

failure mechanisms were assigned to these stress states and not ductile ones, which would have lower stress levels in the RT stress plane and would, thus, lie right within all other ductile failure stress states.

4.2. Determination of failure surfaces at clear-wood scale

With this identification of failure mechanisms a new multisurface failure criterion can be defined, now with surfaces defining ideal plasticity under compression and crack initiation under tension, where to each crack initiation surface a different effective crack direction is assigned to. First, to all simulation results either a ductile or a brittle failure mechanism was assigned to. Like in [26], for the classification of, especially the brittle, failure mechanisms, the main focus is on the radial-tangential stress plane. This can be legitimized by the structural features of wood on its lower length scales with long wood fibers and, thus, its resemblance to a unidirectional fiber reinforced composite. Primarily the huge difference in strength values between grain and perpendicular-to-grain directions (with the former one being more than a magnitude higher) leads, for brittle failure, to two main types of failure: fiber rupture normal to the fiber direction and failure parallel to the fiber direction. As for the latter one we only know that the crack plane is parallel to the fiber direction, but the exact orientation of the crack normal is not known, a classification into several global crack directions in the RT-plane is needed.

Fig. 9 shows those failure stress states in the RT-plane, which exhibit low shear stress components and low stress in longitudinal direction, respectively. Blue points indicate simulation results with ductile failure mechanisms, whereas the red, green and orange ones show brittle failure. Here, it already can be noticed that for the latter ones, all brittle failure mechanisms in the RT-plane were classified into one of three main failure types: for the red points, marked with 1, the normal vector of its global crack direction shows in tangential direction (cf. red lines in Fig. 5(a)), for the orange points (2) a normal vector showing in radial direction was chosen and for the green ones (3) the normal vector is equal to the normalized combination of the radial and tangential unit vectors.

The failure criterion of Tsai and Wu in the following form is used to define a multisurface failure criterion at the clear-wood level:

$$f_i^{TW,cw}(\boldsymbol{\sigma}) = a_{LL,i}\,\sigma_{LL} + a_{RR,i}\,\sigma_{RR} + a_{TT,i}\,\sigma_{TT} + b_{LLLL,i}\,\sigma_{LL}^2 + b_{RRRR,i}\,\sigma_{RR}^2 + b_{TTTT,i}\,\sigma_{TT}^2 + 2\,b_{RRTT,i}\,\sigma_{RR}\,\sigma_{TT} + 4\,b_{LRLR,i}\,\tau_{LR}^2 + 4\,b_{RTRT,i}\,\tau_{RT}^2 + 4\,b_{TLTL,i}\,\tau_{TL}^2 \leqslant 1 \tag{22}$$

For the definition of the failure surfaces in the RT-plane the tensor components $a_{RR,i}$, $a_{TT,i}$, $b_{RRRR,i}$, $b_{TTTT,i}$ and $b_{RRTT,i}$ are identified for each failure mode. The failure stress states of the ductile failure mechanisms in Fig. 9 represent the before mentioned state of fully plastified EW layers and, thus, the points marked with circles in Fig. 5(a). Due to the not yet implemented hard-

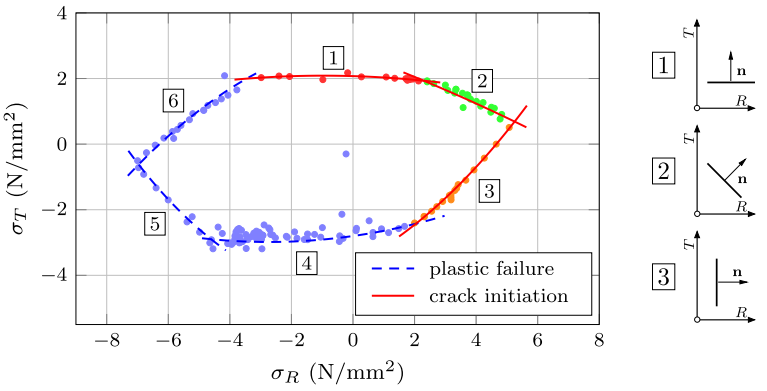

Fig. 9. Failure surfaces for the annual ring unit cell in the σ_R-σ_T plane, with blue surfaces identifying ductile and red ones brittle failure mechanisms, and for latter ones assigned crack directions after crack initiation are shown. (For interpretation of the references to colour in this figure legend, the reader is referred to the web version of this article.)

ening effects into the earlier described multisurface algorithm, these stress states were chosen for the fitting of the failure surfaces. By not allowing hardening to take place, especially under combined compression in R- and T-directions, the corresponding stress values will be underestimated in corresponding simulations, which must be kept in mind in the evaluation process. Anyhow, to allow an straightforward implementation of a second set of surfaces, representing the fully plastified state at the end of possible hardening behavior, now three failure surfaces in the RT-plane are chosen to describe plastic failure mechanisms. These surfaces (4, 5 and 6) are shown in Fig. 9 with dashed blue lines. In addition, the abovementioned three failure mechanisms describing brittle failure are depicted by solid red lines and the corresponding crack normal vectors, which are assigned to these surfaces, can be seen on the right of Fig. 9.

After the determination of the Tsai-Wu tensor components of the failure surfaces in the RT-plane, now, the corresponding components in L-direction $a_{LL,i}$ and $b_{LLLL,i}$ are fitted to the failure stress states by lifting the restriction of the stresses being close to zero in L-direction and fixing the previously determined tensor components. Further, one additional failure surface each for the compression and tension part in L-direction is introduced and denoted with 7 and 8, respectively, in Fig. 10, which shows the multisurface failure criterion in the σ_L-σ_R-σ_T plane, with now only the shear stresses being equal to zero. For the identification of the fourth brittle failure surface, again only failure stress states with the same failure mechanism were used, in this case the ones denoted by a red circle in Fig. 5(a), which indicates a global crack direction parallel to the RT-plane. Thus, failure surface 7 also acts as a crack initiation surface to which a crack normal direction parallel to the L-direction is assigned to.

For the determination of the Tsai-Wu tensor components $b_{LRLR,i}$, $b_{RTRT,i}$ and $b_{TLTL,i}$ representing the shear behavior, for the sake of simplification in this first determination of multiple failure surfaces the same values were chosen for all surfaces by evaluating the maximum values occurring during all unit cell simulations.

An overview of the determined Tsai-Wu tensor components for all clear-wood failure surfaces $f_i^{TW,cw}$ and their distinction into plastic and crack initiation surfaces can be found in Table 1.

5. Application to clear-wood scale

The developed multisurface failure criterion for clear-wood is now compared to experiments with biaxial loading states, before it is applied to a timber engineering example, where clear-wood is modeled homogeneously.

5.1. Comparison to biaxial experiments

Eberhardsteiner [6] conducted an extensive set of experiments on defect-free spruce samples by applying biaxial loadings in the R-L plane under various grain angle configurations. The latter describes the angle between the longitudinal fiber

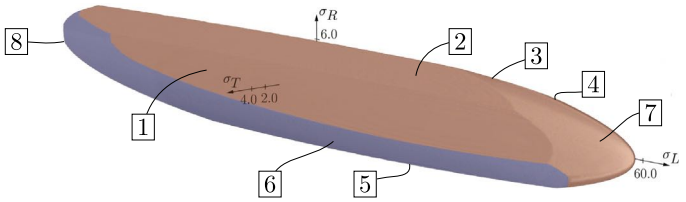

Fig. 10. 3D representation of the failure surfaces in the σ_L-σ_R-σ_T stress space with the shear stresses being equal to zero ($\tau_{LR} = \tau_{LT} = \tau_{RT} = 0$).

Table 1
Tsai-Wu tensor components and type of failure for all clear-wood failure surfaces $f_i^{TW,cw}$.

Surface	Type	$a_{LL,i}$	$a_{RR,i}$	$a_{TT,i}$	$b_{LLLL,i}$	$b_{RRRR,i}$	$b_{TTTT,i}$	$b_{RRTT,i}$	$b_{LRLR,i}$	$b_{RTRT,i}$	$b_{TLTL,i}$
1	Crack	−0.00414	0.01173	0.47073	0.00008	0.00713	0.00559	0.00048	0.01235	0.01563	0.00826
2	Crack	−0.00370	0.12170	0.34478	0.00008	0.00405	0.00541	0.00138	0.01235	0.01563	0.00826
3	Crack	−0.00240	0.11788	−0.25892	0.00007	0.02081	0.00357	−0.00231	0.01235	0.01563	0.00826
4	Plastic	−0.00357	0.04885	−0.34852	0.00013	0.00890	0.00299	0.00002	0.01235	0.01563	0.00826
5	Plastic	0.00029	−0.01561	−0.18639	0.00011	0.01591	0.00517	0.00024	0.01235	0.01563	0.00826
6	Plastic	−0.00876	−0.03995	0.31830	0.00020	0.01897	0.00001	0.00000	0.01235	0.01563	0.00826
7	Crack	−0.02167	−0.00909	−0.10714	0.00008	0.00909	0.03571	0.00000	0.01235	0.01563	0.00826
8	Plastic	0.01452	0.03409	0.03333	0.00006	0.01136	0.03333	0.00000	0.01235	0.01563	0.00826

direction and the principal stress σ_1. The resulting comprehensive data set for multiaxial failure stress states is now compared to the new multisurface failure criterion, which is shown in Fig. 11. Here, both experimental and numerical results for two grain angles are plotted for the principal stresses σ_1 and σ_2, respectively. As the test setup of the experimentally tested spruce samples with the dimension in tangential direction being more than a magnitude smaller than in the other two directions resembles a plate, a plane stress conditions can be assumed. Thus, for the evaluation of the failure surfaces only σ_{LL}, σ_{RR} and τ_{LR} are not equal to zero.

Comparisons of preliminary XFEM simulation results in [9] to the same experiments have already shown that those were in good agreement with the experimental results. The results for a grain angle of 0° are shown in Fig. 11(a). In σ_2-direction the crack initiation surfaces agree perfectly with the experimentally obtained effective failure stress states and the plastic failure surfaces enclose the experimental results. In direction of the principal stress σ_1, the crack initiation surface lies in the middle of the experimental values, whereas the ductile failure stress states are slightly underestimated. For the second configuration of 45° (see Fig. 11(b)), the crack initiation surfaces are slightly within the experimental values in the lower right corner. Again, in this region some experimental scatter can be noticed as well as at the right intersection of crack initiation and plastic failure surfaces.

Although the tested samples were defect-free, up to a point where at least with the naked eye no inhomogeneities could be observed, wood is still a natural material. Thus, the observable scatter of the experimentally obtained effective strength values, especially under tension in longitudinal direction, can, on one hand, be explained by defects on several (lower) length scales, causing this variation for the brittle failure mechanisms. On the other hand, in the experiments the density alone varied from 0.36 to 0.63 g/cm^3, whereas the homogenized density of the simulated clear-wood material was approximately 0.46 g/cm^3 [24].

Still, in general, it can be confirmed that in stress regions, where brittle failure is expected, the corresponding surfaces are on the lower end of the experimental results (e.g. see Fig. 11(b)), as already has been observed in Füssl et al. [9]. Under compression, the future implementation of hardening effects should also lead to even better results in the corresponding stress regions, where the assumption of perfect plasticity should lead to the formation of an outer envelope of the experimental results, like shown in [9]. With this comparison, the capability of the multisurface to capture both brittle and ductile failure

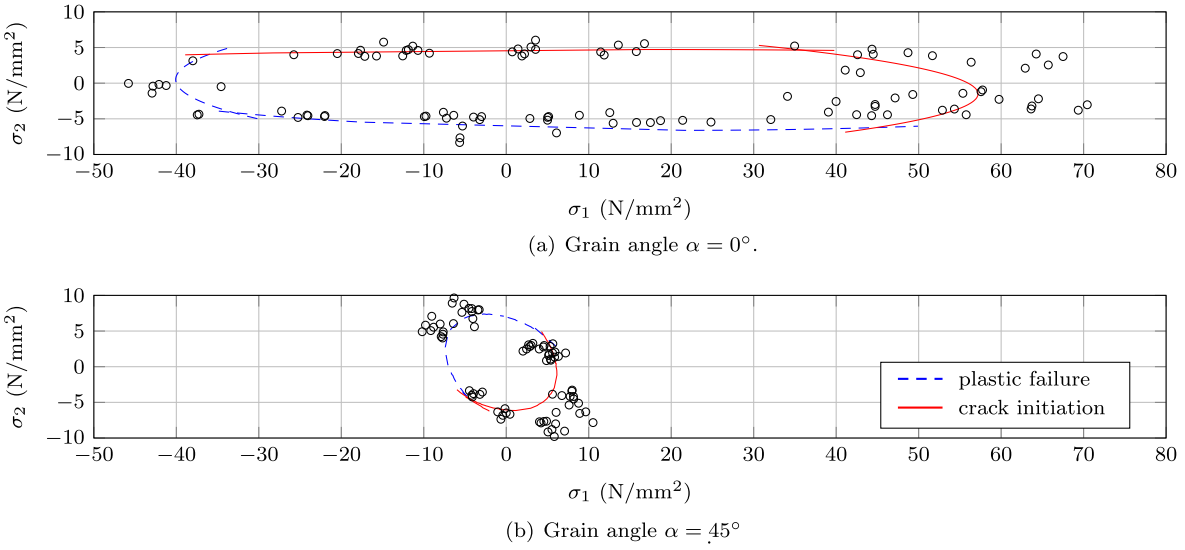

(a) Grain angle $\alpha = 0°$.

(b) Grain angle $\alpha = 45°$

Fig. 11. Failure stress states of clear-wood in the σ_L-σ_R plane for two different grain angles. Comparison of experimental results from [6] and the presented multisurface failure criterion.

mechanisms can be confirmed for several experimental configurations. Once again it must be emphasized that no empirical calibration has been performed on any length scale.

5.2. Dowel-type timber connection

For the application of the multisurface failure criterion to a timber engineering example, the embedment behavior of a single-dowel connection test [21] is simulated.

5.2.1. Materials and method

Following DIN EN 383 [4], geometry and dimensions of the tested specimen were chosen for a so-called full-hole test, shown in Fig. 12(a). This means that into a straight-grained section of Norway spruce with dimensions of $100 \times 65 \times 30\,\text{mm}^3$ (L × T × R) a 12 mm bore hole was drilled at a height of 67.5 mm. For the material properties, wood was modeled homogeneously, not taking into account the annual year rings. For the sake of convenience, a Cartesian orthotropic coordinate system was chosen, implying parallel annual year rings, which is a fair assumption for cross sections with rather big distances to the pith. The orthotropic material properties were determined by means of a micromechanical model developed by Hofstetter et al. [14], resulting in a homogenized stiffness tensor for clear wood with a density of 450 kg m^{-3}:

$$\mathbb{C}_{cw} = \begin{bmatrix} C_{rrrr} & C_{rrtt} & C_{rrll} & & & \\ & & C_{tttt} & C_{ttll} & & \\ & & C_{llll} & & & \\ & & & C_{rtrt} & & \\ & \text{sym.} & & & C_{rlrl} & \\ & & & & & C_{tltl} \end{bmatrix} = \begin{bmatrix} 13,556 & 307 & 245 & & & \\ & 946 & 411 & & & \\ & & 644 & & & \\ & & & 104 & & \\ & \text{sym.} & & & 636 & \\ & & & & & 648 \end{bmatrix} [\text{MPa}] \tag{23}$$

All steel components had a Young's modulus of 210,000 MPa and a Poisson's ratio of 0.3.

The 3D wood sample is fixed at the bottom surface and the two steel plates move vertically in a displacement controlled manner downwards. The load is then transferred from the steel plates via semi-circular cut-outs to the 12 mm steel dowel. The corresponding surface interaction was defined as a hard contact relationship with a friction coefficient of 0.7. For the contact behavior between steel dowel and wood the normal behavior was controlled with a pressure-overclosure relationship and the tangential one by chosing a friction coefficient of 0.3.

The simulations were realized via 8-node linear brick elements with the minimum (around the bore hole) and maximum (at all other specimen edges) element edge seed size being 1.0 and 5.0 mm (see Fig. 12(b)).

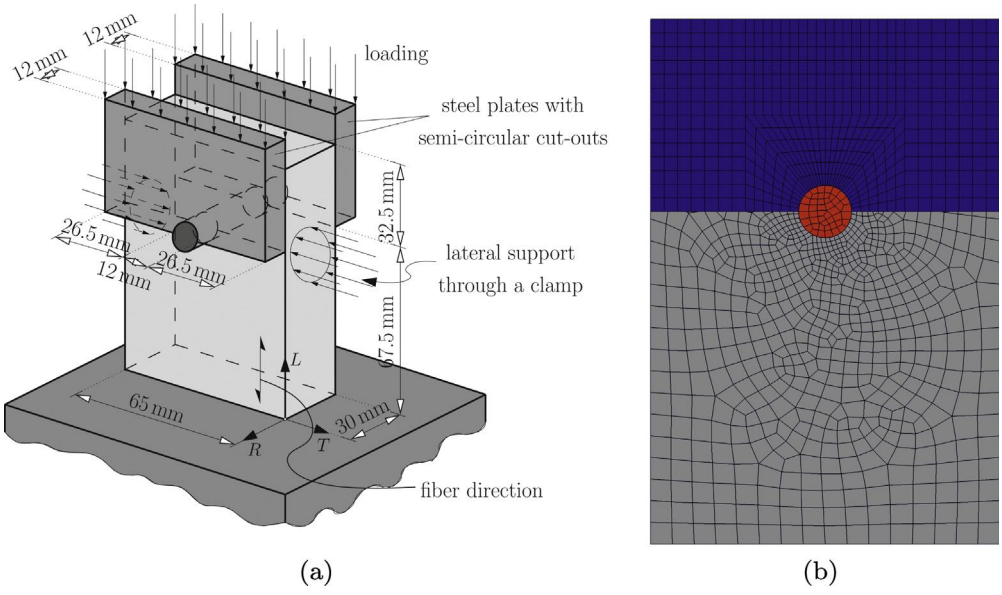

Fig. 12. (a) Experimental setup for the dowel-type connection test [21] and (b) front view of the used FE model, showing mesh details (gray = spruce wood, red = steel dowel, blue = steel plate). (For interpretation of the references to colour in this figure legend, the reader is referred to the web version of this article.)

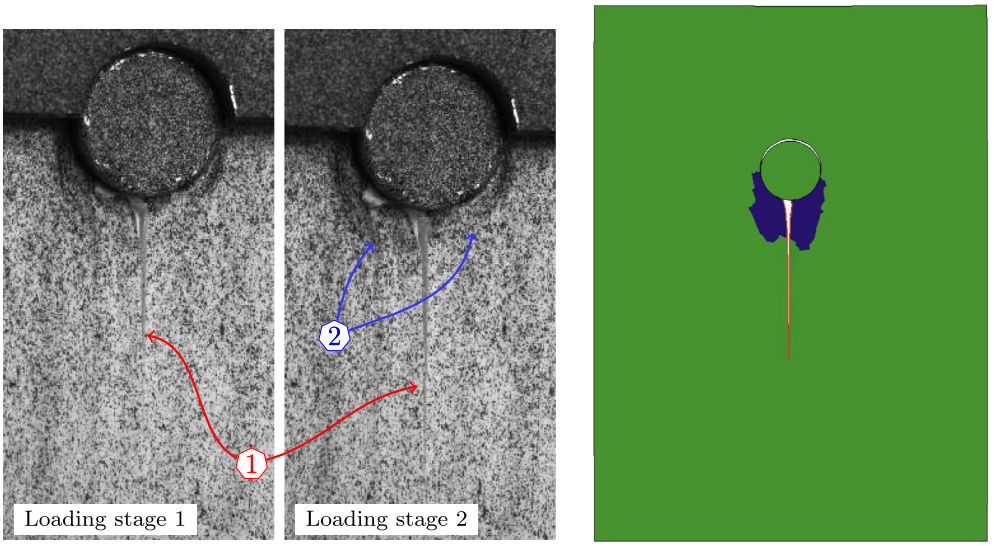

Fig. 13. (a) Comparison of two loading stages of the corresponding experiment [21], where ① shows the propagating crack and ② the densification of wood material due to embedment pressure, and (b) Simulation results with plastified regions (blue) and the developed crack underneath the dowel (red) (with the steel plate not displayed and a deformation scale factor of 5). (For interpretation of the references to colour in this figure legend, the reader is referred to the web version of this article.)

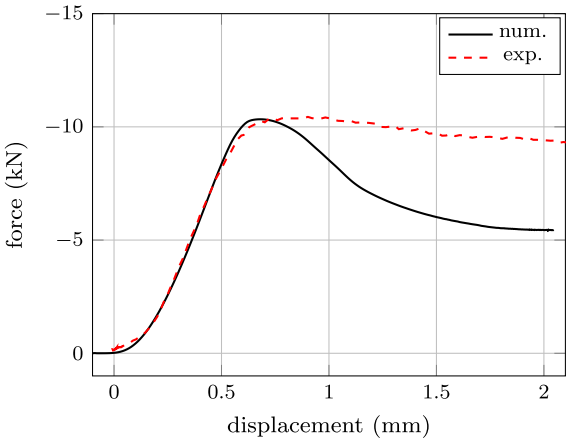

Fig. 14. Experimentally [21] (dashed, red curve) and numerically (solid, black curve) obtained load-displacement curves. (For interpretation of the references to colour in this figure legend, the reader is referred to the web version of this article.)

5.2.2. Comparison of simulation and experimental results

Fig. 13(a) shows close-ups of the experimental tests for two different loading stages (noticable by the movement of the steel parts). As the dowel moves downwards, the wood specimen is exposed to corresponding embedment pressure. This leads to compressive stress in vertical and, thus, longitudinal material direction, but also to perpendicular-to-grain tension. As the strength for the latter one is significantly lower, a vertical crack starts to form below the dowel. Then, almost simultaneously the crack propagates in vertical direction (marked with ①) and plastification-like effects, starting close to the dowel-wood contact region, can be observed. In Fig. 13(a), the latter effect can be noticed by a densification of the black and white spray speckle pattern, marked with ②. The same failure mechanisms can be reproduced very well by the developed model (see Fig. 13(b)). Furthermore, by comparing the experimentally and numerically obtained load-displacement curves (see Fig. 14), the model's capability to estimate the load peak can be confirmed. The lower post-peak load level in the simulation might be explained by the missing implementation of hardening effects.

In summary, it can be noted that the simulation tool is now capable of representing both plastic failure mechanisms and the formation of cracks at the same time and in the same regions.

6. Conclusions

A multisurface failure criterion for clear-wood was developed by applying two previously proposed failure criteria for late- and earlywood on a finite element unit cell at the annual year ring scale. Here, the repetitive layered structure was modeled with the mentioned two layers, by assuming homogeneous material properties and a parallel layout. By using a newly implemented algorithm the layers' failure criteria could cover both ductile and brittle failure mechanisms. Thus, to identify all possible failure modes of clear wood, a sampling technique was used to obtain a total of 1000 loading combinations, which were applied to three versions of FE models, which differ in the position of a predefined defect acting as a starting point in case of brittle failure mechanisms.

The resulting failure mechanisms could be distinguished into two groups: ductile and brittle ones. For the first ones, under pure compressive loading in each of the two perpendicular-to-grain directions, almost no non-linear behavior could be noticed and the whole model went from a linear elastic to a perfectly plastic stress state under only little additional loading. Under combined compression in radial and tangential direction a clear non-linear behavior could be observed in the stress/strain curves before the entire model was plastified. During this hardening period the effective stresses could be almost doubled. For the second class of failure mechanisms, the brittle ones, clear global/effective crack directions could be obtained. To reduce the final number of failure surfaces, these failure mechanisms were classified into three different global crack directions: two with crack normals showing in radial and tangential direction, respectively, under tension in the same direction and a third class with a crack normal with an angle between these two directions for combined tensile loading in both directions.

In addition to the previous validation of failure mechanisms and crack patterns at the annual ring scale [24], now, the comparisons of the new multisurface failure criterion to an extensive set of experiments of clear-wood spruce samples in the LR-plane [6] showed that both ductile and brittle failure mechanisms can be predicted very well. Furthermore, the application of the model to a dowel-type timber connection confirmed the tool's capability to represent both plastic failure and the development of cracks at the same time even in confined regions. Thus, in general, the combination of failure surfaces inducing perfect plasticity and of crack initiation surfaces within a single failure criterion leads to a powerful tool for the description of complex failure mechanisms in various timber engineering applications. Therefore, this modeling approach, which considers structural features on several lower length scales and does not need any calibration of material parameters on the higher length scales, seems to be very promising.

The next steps in the enhancement of the failure criterion will be an implementation of the hardening behavior under compressive loading and the consideration of the failure surfaces' dependence on density and other material parameters with high variation within clear-wood. The combination of this new failure criterion with previous developments of a numerical simulation tool for wooden boards [23,25], which is able to consider morphological features at the single board level, like knot inclusions and fiber deviations in their vicinities, enables realistic simulations of complex failure mechanisms of not only single wooden boards but also more complex wood-based products, like Glulam and CLT elements [13]. In this case, an extension of the presented multiscale concept by other numerical methods, like limit analysis [22,10], and by taking stochastic aspects [9,16] into account will be performed. Furthermore, the simulation tool can be used in the development of new wood composites, by making the material wood more predictable and, thus, more interesting for engineering applications. Such simulations and developments should serve as basis for improved design concepts, the development of new and improvement of existing wood-based products, and could, finally, raise confidence in wood to a level where it should be.

Acknowledgements

Promoted out of funds of the City Council of Vienna by Vienna Business Agency. A trust of Vienna City council.

References

[1] Blanco C, Cabrero J, Martin-Meizoso A, Gebremedhin K. Design oriented failure model for wood accounting for different tensile and compressive behavior. Mech Mater 2015;83(Apr.):103–9. ISSN: 0167-6636 http://www.sciencedirect.com/science/article/pii/S0167663615000022.
[2] Böhm HJ. A short introduction to continuum micromechanics. Springer; 2004.
[3] Danielsson H, Gustafsson PJ. Fracture analysis of glued laminated timber beams with a hole using a 3d cohesive zone model. Eng Fract Mech 2014;124:182–95. ISSN: 0013-7944 http://www.sciencedirect.com/science/article/pii/S0013794414001313.
[4] DIN EN 383. Holzbauwerke – Prüfverfahren – Bestimmung der Lochleibungsfestigkeit und Bettungswerte für stiftförmige Verbindungsmittel, 3; 2007 [in German].
[5] Dourado N, Morel S, De Moura M, Valentin G, Morais J. Comparison of fracture properties of two wood species through cohesive crack simulations. Compos Part A: Appl Sci Manuf 2008;39(2):415–27. ISSN: 1359-835X.
[6] Eberhardsteiner J. Mechanisches Verhalten von Fichtenholz: Experimentelle Bestimmung der biaxialen Festigkeitseigenschaften. New York: Springer Wien; 2002 [in German].
[7] Fournier CR, Davids WG, Nagy E, Landis EN. Morphological lattice models for the simulation of softwood failure and fracture. Holzforschung 2007;61(4):360–6. ISSN: 1437-434X.
[8] Frühmann K, Burgert I, Stanzl-Tschegg S, Tschegg E. Mode i fracture behaviour on the growth ring scale and cellular level of spruce (picea abies [l.] karst.) and beech (fagus sylvatica l.) loaded in the tr crack propagation system. Holzforschung 2003;57(6):653–60.
[9] Füssl J, Kandler G, Eberhardsteiner J. Application of stochastic finite element approaches to wood-based products. Arch Appl Mech 2016;86(1–2):89–110. ISSN: 0939-1533.
[10] Füssl J, Li M, Lukacevic M, Eberhardsteiner J, Martin C. Comparison of unit cell-based computational methods for predicting the strength of wood. Eng Struct; 2017. submitted for publication.

[11] Guindos P. Method for the integral calculation of the fiber orientation and the fundamental material properties of softwood logs and lumber. Holzforschung 2016;70(10):981–91. ISSN: 1437-434X.
[12] Hackspiel C, Borst K, Lukacevic M. A numerical simulation tool for wood grading model development. Wood Sci Technol 2014;48(3):633–49. ISSN: 0043-7719 http://dx.doi.org/10.1007/s00226-014-0629-0.
[13] Hochreiner G, Füssl J, Eberhardsteiner J. Cross-laminated timber plates subjected to concentrated loading. Strain 2014;50(1):68–81. ISSN: 1475-1305.
[14] Hofstetter K, Hellmich C, Eberhardsteiner J. Development and experimental validation of a continuum micromechanics model for the elasticity of wood. Eur J Mech A/Solids 2005;24:1030–53.
[15] Jenkel C, Kaliske M. Finite element analysis of timber containing branches – an approach to model the grain course and the influence on the structural behaviour. Eng Struct 2014;75:237–47.
[16] Jenkel C, Leichsenring F, Graf W, Kaliske M. Stochastic modelling of uncertainty in timber engineering. Eng Struct 2015;99(Sept.):296–310. ISSN: 0141-0296 http://www.sciencedirect.com/science/article/pii/S0141029615003053.
[17] Keunecke D, Stanzl-Tschegg S, Niemz P. Fracture characterisation of yew (taxus baccata l.) and spruce (picea abies [l.] karst.) in the radial-tangential and tangential-radial crack propagation system by a micro wedge splitting test. Holzforschung 2007;61(5):582–8. ISSN: 1437-434X.
[18] Landelius J. Finit area metoden. en bra metod för beräkning av uppfläkningsbrott? Rep. No. TVSM, 5043:66; 1989 [in Swedish].
[19] Landis EN, Navi P. Modeling crack propagation in wood and wood composites. a review. cost action e35 2004-2008: wood machining – micromechanics and fracture. Holzforschung 2009;63(2):150–6.
[20] Landis EN, Vasic S, Davids WG, Parrod P. Coupled experiments and simulations of microstructural damage in wood. Exp Mech 2002;42(4):389–94. ISSN: 1741-2765 http://dx.doi.org/10.1007/BF02412143.
[21] Lederer W, Bader T, Muszynski L, Eberhardsteiner J. Exploring a multi-modal experimental approach to investigation of local embedment behavior of wood under steel dowels. Strain 2016. doi: http://dx.doi.org/10.1111/str.12199.
[22] Li M, Füssl J, Lukacevic M, Martin C. A numerical limit analysis approach for strength predictions of wood. Int J Solids Struct; 2017. submitted for publication.
[23] Lukacevic M, Füssl J. Numerical simulation tool for wooden boards with a physically based approach to identify structural failure. Eur J Wood Wood Prod 2013;72(4). doi: http://dx.doi.org/10.1007/s00107-014-0803-y.
[24] Lukacevic M, Füssl J. Application of a multisurface discrete crack model for clear wood taking into account the inherent microstructural characteristics of wood cells. Holzforschung 2016;70(9):845–53. doi: http://dx.doi.org/10.1515/hf-2015-0162.
[25] Lukacevic M, Füssl J, Griessner M, Eberhardsteiner J. Performance assessment of a numerical simulation tool for wooden boards with knots by means of full-field deformation measurements. Strain 2014;50(4):301–17.
[26] Lukacevic M, Füssl J, Lampert R. Failure mechanisms of clear wood identified at wood cell level by an approach based on the extended finite element method. Eng Fract Mech 2015;144:158–75. ISSN: 0013-7944 http://www.sciencedirect.com/science/article/pii/S001379441500332X.
[27] Mackenzie-Helnwein P, Eberhardsteiner J, Mang H. A multi-surface plasticity model for clear wood and its application to the finite element analysis of structural details. Comput Mech 2003;31(1–2 SPEC.):204–18.
[28] Masuda M. Theoretical consideration on fracture criteria of wood dproposal of finite small area theory. In: Proceedings of the 1988 international conference on timber engineering, Seattle, vol. 2; 1998. p. 584–95.
[29] Michel J, Moulinec H, Suquet P. Effective properties of composite materials with periodic microstructure: a computational approach. Comput Methods Appl Mech Eng 1999;172(1):109–43. ISSN: 0045-7825.
[30] Mishnaevsky Jr L, Qing H. Micromechanical modelling of mechanical behaviour and strength of wood: state-of-the-art review. Comput Mater Sci 2008;44(2):363–70. ISSN: 0927-0256 http://www.sciencedirect.com/science/article/pii/S0927025608001882.
[31] Murata K, Nagai H, Nakano T. Estimation of width of fracture process zone in spruce wood by radial tensile test. Mech Mater 2011;43(7):389–96. ISSN: 0167-6636.
[32] Qing H, Mishnaevsky L. A 3d multilevel model of damage and strength of wood: analysis of microstructural effects. Mech Mater 2011;43(9):487–95. ISSN: 0167-6636.
[33] Schmidt J, Kaliske M. Zur dreidimensionalen materialmodellierung von fichtenholz mittels eines mehrflächen-plastizitätsmodells. Holz als Roh- und Werkstoff 2006;64(5):393–402. ISSN: 0018-3768 http://dx.doi.org/10.1007/s00107-006-0102-3.
[34] Schmidt J, Kaliske M. Simulation of cracks in wood using a coupled material model for interface elements. Holzforschung 2007;61(4).
[35] Serrano E, Gustafsson J. Fracture mechanics in timber engineering – strength analyses of components and joints. Mater Struct 2006;40:87–96.
[36] Simo JC, Hughes TJ. Computational inelasticity. New York: Springer; 1998.
[37] Sjödin J, Serrano E. A numerical study of methods to predict the capacity of multiple steel-timber dowel joints. Holz als Roh- und Werkstoff 2008;66(6):447–54.
[38] Sjödin J, Serrano E, Enquist B. An experimental and numerical study of the effect of friction in single dowel joints. Holz als Roh- und Werkstoff 2008;66(5):363–72.
[39] Suquet P. Continuum micromechanics. Springer-Verlag New York, Inc.; 1997.
[40] Tsai SW, Wu EM. A general theory of strength for anisotropic materials. J Compos Mater 1971;5(1):58–80. ISSN: 0021-9983.